

Ising and XY paramagnons in two-dimensional 2H-NbSe₂

A. T. Costa,¹ M. Costa,² and J. Fernández-Rossier^{1,*}

¹*QuantaLab, International Iberian Nanotechnology Laboratory (INL),
Av. Mestre José Veiga, 4715-330 Braga, Portugal*

²*Instituto de Física, Universidade Federal Fluminense, 24210-346, Niterói, RJ, Brazil*
(Dated: March 4, 2022)

Paramagnons are the collective modes that govern the spin response of nearly magnetic conductors. In some cases they mediate electron pairing leading to superconductivity. This scenario may occur in 2H-NbSe₂ monolayers, that feature spin-valley coupling on account of spin-orbit interactions and their lack of inversion symmetry. Here we explore spin anisotropy of paramagnons both for non-centrosymmetric Kane-Mele-Hubbard models for 2H-NbSe₂ monolayers described with a DFT-derived tight-binding model. In the infinite wavelength limit we find spatially uniform paramagnons with energies around 1 meV that feature a colossal off-plane uniaxial magnetic anisotropy, with quenched transversal spin response. At finite wave vectors, longitudinal and transverse channels reverse roles: XY fluctuations dominate within a significant portion of the Brillouin zone. Our results show that 2H-NbSe₂ is close to a Coulomb-driven in-plane (XY) spin density wave instability.

PACS numbers:

A nearly magnetic conductor is a material on the brink of a quantum phase transition to a magnetically ordered state. The transition is controlled by the Stoner parameter, defined as the product of the atomic Coulomb repulsion U and the density of states at the Fermi energy, ρ_0 . As it happens in conventional phase transitions, fluctuations are enhanced due to proximity to the critical point. In the case of nearly ferromagnetic conductors, spin fluctuations are enhanced when $\rho_0 U \simeq 1$, leading to the emergence of paramagnons, prominent features in the low energy spectra, that anticipate the formation of magnon resonances at the other side of the transition. The formation of paramagnons occurs for all magnetic instabilities, either ferromagnetic, antiferromagnetic, or spin-density wave, and lead to diverging magnetic responses at specific wave-vectors that characterize the ordered phase at the other side of the transition. [1].

Interaction of paramagnons with quasiparticles lead to observable effects, such as the renormalization of the quasiparticle effective mass [2] and a resulting enhancement of the electrical resistivity [3] and electronic specific heat [2, 4]. Ferromagnetic spin fluctuations can also result in p-wave triplet pairing[5, 6], that could lead to the coexistence of triplet SC and FM, or the emergence of SC order in the vicinity of a FM phase transition. The interplay between superconductivity and ferromagnetic spin fluctuations has been explored in materials like Pd[7], ZnZr₂[8], liquid ³He, twisted bilayer graphene[9–11], ABC graphene trilayer[12, 13], UTe₂[14], and 2H-NbSe₂[15–17]. Whereas most of these materials are centro-symmetric and spin-orbit coupling (SOC) has a minor impact and is customarily neglected, the case of 2H-NbSe₂ monolayers is very different.

Spin-orbit interaction has a dramatic effect on the energy bands of two-dimensional 2H-NbSe₂ and related transition metal dichalcogenide (TMD) monolayers[18,

19]. The lack of inversion symmetry leads to a momentum-dependent spin splitting of the energy bands. The splitting is large, on account of the strong SOC of the transition metal. As a result, Kramers doublets have their momenta at opposite points in the Brillouin zone (see Fig. 1). For the states at the corner points of the BZ, the so-called valleys, this phenomenon is the celebrated spin-valley coupling, that leads to a peculiar band structure, with two pockets that feature complete and opposite spin polarizations.

In this paper, we study spin fluctuations in spin-valley coupled systems. From inspection of their energy bands we can expect a very anisotropic spin response. When the Fermi energy lies in the half-metallic pockets at the top of the valence band (see Fig. 1), spin-flip fluctuations are gapped for $q = 0$, in contrast with longitudinal spin-conserving fluctuations. This effect also occurs when the Fermi surface is no longer at the valleys, but still in the spin-split region. The first case is relevant for 2H-MoS₂, for which a doping induced ferromagnetic transition has been reported[20], and other semiconducting TMDs. The second case is relevant for 2H-NbSe₂. To study this phenomenon, we compute spin fluctuations using the Random Phase Approximation (RPA) for two types of Hamiltonians. First, we consider the Kane-Mele-Hubbard model[21–24] with a sublattice potential term that breaks inversion symmetry, leading to spin-valley coupled bands. Second, we consider a multi-orbital effective Hamiltonian (tight-binding like) obtained from DFT calculations describing a monolayer of 2H-NbSe₂.

The spin susceptibility, that governs the non-local spin response to magnetic perturbations, is given by

$$\chi_{ab}^{\eta\eta'}(\vec{r}, \vec{r}', t) = -i\theta(t) \left\langle \left[S_a^\eta(\vec{r}, t), S_b^{\eta'}(\vec{r}', 0) \right] \right\rangle, \quad (1)$$

where $a, b = x, y, z$ label the spin channel, and η, η' label the atomic orbitals inside the unit cell. In the frequency-

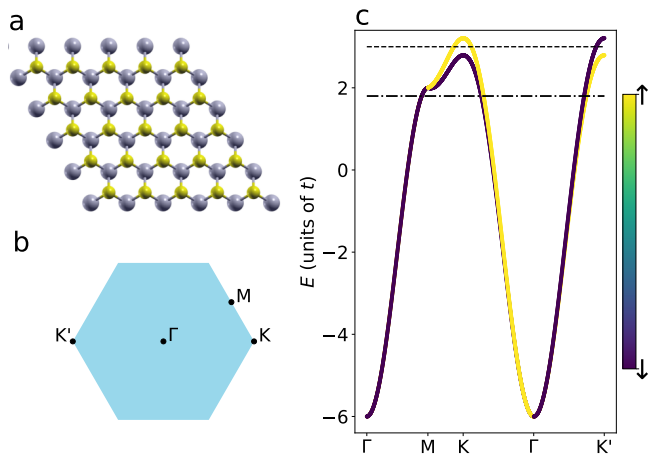


FIG. 1: a) NbSe₂ honeycomb lattice (HCL) with broken inversion symmetry. b) Brillouin zone of the HCL displaying the relevant high-symmetry points. c) Band structure of the extended Kane-Mele model with $\Delta \rightarrow \infty$ and finite SOC ($t_{KM} = 0.04t$). The two horizontal lines mark the values of E_F used in the calculations of the spin fluctuation spectra displayed in Fig. 2. Dashed line: $E_F = 3t$, dot-dashed line: $E_F = 1.8t$.

momentum domain we have

$$\chi_{ab}^{\eta\eta'}(\vec{q}, \omega) = \int_{-\infty}^{\infty} dt e^{i\omega t} \int d\vec{r} e^{i\vec{q}\cdot\vec{r}} \chi_{ab}^{\eta\eta'}(\vec{r}, 0, t) \quad (2)$$

In the following we compute the spin-response in the RPA approximation,

$$\chi = [1 - U\chi_0]^{-1} \chi_0 \quad (3)$$

where χ_0 is the non-interacting ($U = 0$) spin susceptibility tensor, for which closed analytical expressions are readily obtained in terms of the single-particle states and energies. Therefore, equation (3) permits one to obtain the spin response including the effect of the interactions in the RPA[25, 26]. For systems with spin rotational invariance, such as paramagnets without spin-orbit coupling, the spin response matrix is proportional to the unit matrix in the spin index. Therefore, the spin response is the same in all directions. Here we study the case where spin rotational invariance is broken in the paramagnetic phase, due to SOC.

We now apply this formalism to an extended Kane-Mele Hubbard model on a bipartite honeycomb lattice[21–24]. This is a toy model for a TMD. We assume that the A triangular sublattice of the honeycomb hosts the Nb atom, whereas the B sublattice contains a non-interacting site. The Hamiltonian is given by

$$H = H_0 + H_{SOC} + \frac{\Delta}{2} \sum_{i\sigma} \tau_i^z c_{i\sigma}^\dagger c_{i\sigma} + U \sum_{i \in A} n_{i\uparrow} n_{i\downarrow} \quad (4)$$

where H_0 describes first and second neighbors hopping in

a honeycomb lattice, H_{SOC} is the Kane-Mele SOC[27],

$$H_{SOC} = it_{KM} \sum_{\langle\langle i,j \rangle\rangle, \sigma} \sigma c_{i,\sigma}^\dagger \hat{z} \cdot (\mathbf{d}_{kj} \times \mathbf{d}_{ik}) c_{j,\sigma} \quad (5)$$

where $\langle\langle i, j \rangle\rangle$ denotes a sum over all pairs of second neighbors i, j , in the honeycomb lattice, and \mathbf{d}_{kj} (\mathbf{d}_{ik}) are the unit vectors going from site k (i) to site j (k), where k labels the common first neighbor of sites i and j [27]. The main role of $\hat{z} \cdot (\mathbf{d}_{kj} \times \mathbf{d}_{ik})$ is to make the SOC term odd under spatial inversion and with opposite sign at each sublattice, for a given direction.

If we take $U = \Delta = 0$ this term opens up a topological gap at the Dirac point. However, here we include a sublattice potential, $\frac{\Delta}{2} \tau_i^z$, where $\tau_i^z = \pm 1$ for $i = A, B$. [27] This breaks inversion symmetry, opens up a trivial gap when $\Delta \gg t_{KM}$ and, combined with the SOC term, leads to a spin splitting of the bands, as described above. This makes our model different from the case with inversion symmetry[23, 24]. Since fluctuating moments are expected to be hosted by the Nb atoms, we consider a model where Hubbard U interactions are only active in one sublattice.

In the non-interacting limit ($U = 0$), the energy bands of the Hamiltonian capture the main features of TMD monolayers: a gap separates a valence and a conduction band whose extrema are at the K, K' corners of the BZ zone. In the neighborhood of the K, K' points the bands have large spin-splitting and Kramers partners have opposite wave vectors. In this region the bands are well described by a Dirac equation with a mass [18]. The model conserves the spin projection perpendicular to the atomic plane, so that we can still label the single-particle states with $\sigma = \pm 1/2$.

Depending on the location of the Fermi energy, the model can mimic a semiconducting TMD, such as 2H-MoS₂, 2H-MoSe₂, 2H-WSe₂, 2H-WSe₂, doped with either electrons or holes and the Fermi energy close to the band extrema, or 2H-NbSe₂, with the Fermi energy deep down closer to the conduction band's minima. We now study the spin fluctuations in these two limits as a function of the Hubbard interaction U .

We focus first on the $q = 0$ low energy spin fluctuations, that govern the long wavelength spin response of the material. Because of the C_3 symmetry of the honeycomb lattice we have $\chi_{xx} = \chi_{yy} = \chi_{\perp}$. In the non-magnetic phase we have $\chi_{xy} = \chi_{yx} = 0$. Therefore, the spin response is diagonal in the spin index, with two different components for the zz (χ_{\parallel}) and in-plane components. When the Fermi energy is located close to the K, K' points, zero momenta spin-flip fluctuations are strictly forbidden, for energies smaller than the spin-splitting. In that limit, the Fermi surface is formed by spin-polarized pockets, with opposite polarization, at the K and K' points. In contrast, low energy spin conserving fluctuations are allowed. With this in mind, the results

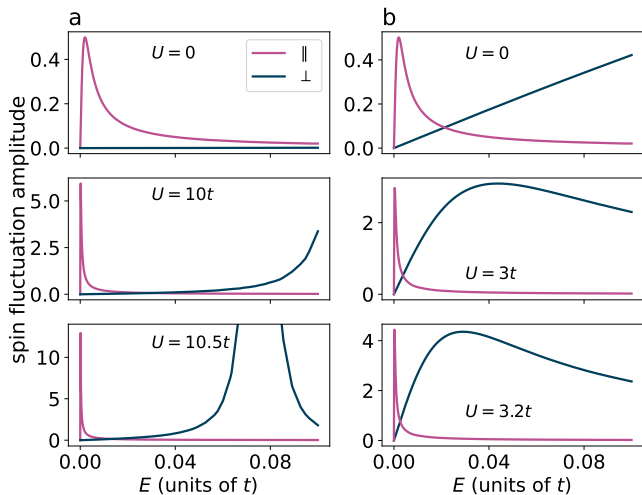


FIG. 2: Spin fluctuation amplitudes at zero wave vector for two Fermi energies: a) $E_F = 3t$ (crossing only spin-split bands), and b) $E_F = 1.8t$ (crossing degenerate spin bands). In both cases the SOC strength is $t_{KM} = 0.04t$. The top row shows the mean-field spin fluctuations. The remaining rows show how the RPA spin fluctuation spectra change as the interaction strength U approaches the critical value. Purple lines correspond to longitudinal fluctuations ($-\Im\chi^{\parallel}/\rho_0$) and dark blue lines correspond to transverse fluctuations ($-\Im\chi^{\perp}/\rho_0$), where ρ_0 is the density of electronic states at the Fermi level, E_F .

of figure 2a, showing a dramatically different behavior for $\chi_{\parallel}(q=0, E)$ and $\chi_{\perp}(q=0, E)$ can be easily understood. It is apparent that, as U increases, the paramagnon peaks only forms on the \parallel or off-plane channel, whereas the transverse spin response is quenched.

We now address the question of whether the strong anisotropy of the spin response is something specific of the states close to the K and K' points, or, on the contrary, the anisotropy also occurs when the Fermi surface has spin-split bands in low symmetry regions of the Brillouin zone. For that matter, we consider now the case where the Fermi energy is located at higher in the valence band (E_F corresponding to the dot-dashed line in figure 1c). In this case we find a smaller value of the critical Stoner parameter $(U\rho_0)_c = 3.3$, that we attribute to a larger density of states. We find the same colossal anisotropy of the low-energy spin fluctuations. We refer to these very anisotropic collective modes as Ising paramagnons. In this case, however, the transverse fluctuations are not as strongly quenched as when E_F only crosses spin-split bands.

We have verified that the anisotropy is driven by the combination of SOC and inversion symmetry breaking. For that matter we have computed the spin response for $\Delta = 0$ and $t_{KM} > 0$. We find that the spin fluctuation spectra along the longitudinal and transverse directions have the same lineshape and virtually identical amplitudes.

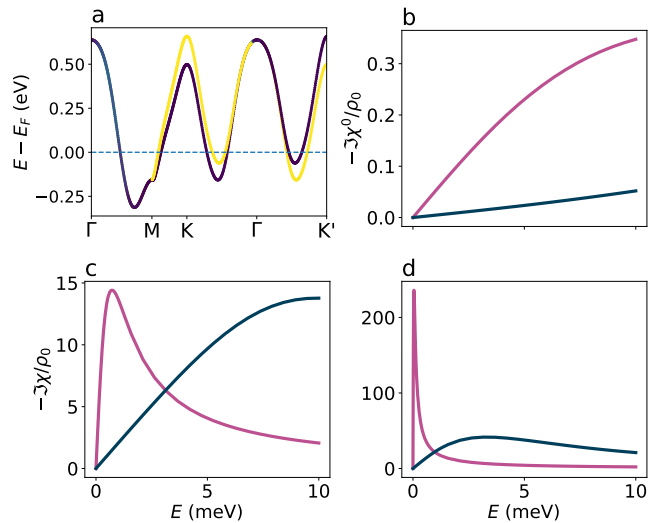


FIG. 3: a) DFT bands for NbSe₂ around the Fermi level. The color code represents the spin projection along z . b) Longitudinal (purple curve) and transverse (dark blue curve) mean-field spin fluctuation spectra at zero wave vector for NbSe₂, extracted from the DFT-based multiorbital TB model. In the lower panels we show the RPA enhanced spin fluctuations for c) $U = 0.86$ eV and d) $U = 0.89$ eV. The critical value for the interaction strength in this case is $U_c = 0.9$ eV.

We now ask whether the same phenomenon holds true for a more realistic Hamiltonian describing 2H-NbSe₂. First we carry out density functional theory (DFT) calculations for the 2H-NbSe₂ [28, 29], using the QUANTUM ESPRESSO suite [30]. The electronic interaction was described within the generalized gradient approximation (GGA) via the Perdew-Burke-Ernzerhof (PBE) functional [31]. Ionic potentials were described by projector augmented-wave (PAW) [32] pseudopotentials available in the 1.0 pslibrary database [33]. The wavefunctions and charge density cutoff energies were 71.5 and 715 Ry, respectively. Full structural optimization was performed until Hellman-Feynman forces were smaller than 0.01 eV/Å with a $13 \times 13 \times 1$ reciprocal space sampling. We found a lattice parameter of 3.47 Å, which is in agreement with other DFT calculations [34]. The Hamiltonian was constructed with a larger K -sampling of $27 \times 27 \times 1$. We allow for spin polarization but the system converged to a non-magnetic ground state. Our results are in line with those obtained in the literature [34]

After the structural optimization, a local effective Hamiltonian was constructed via the pseudo-atomic orbital (PAO) projection method [35, 36] as implemented in the PAOFLOW code [37]. The method consists in projecting the plane wave Kohn-Sham states onto a compact subspace spanned by PAOs already built in the PAW potentials. This procedure reduces the basis set from several thousand plane waves to a few atomic orbital-like basis functions with accuracy comparable to DFT

calculations. In the supplementary material we compare the PAOFLOW and QUANTUM ESPRESSO band structures. The PAW potential for Nb and Se were constructed with a *sspd* and *spd* PAO basis, respectively. This choice results in 13 and 9 orbitals per Nb and Se atom. Obviously, spin-orbit-coupling is essential for spin-splitting at K and K' points. Therefore, we include it as a local term of the form

$$H_{\text{SOC}} = \sum_l \sum_{\mu\nu} \sum_{\sigma, \sigma'=\uparrow, \downarrow} \xi_l (\vec{L} \cdot \vec{S})_{l\mu\sigma, l\nu\sigma'} a_{l\mu\sigma}^\dagger a_{l\nu\sigma'}, \quad (6)$$

where l is an atomic site index, μ, ν are orbital indices, and σ, σ' are spin indices. \vec{L} is the orbital angular momentum operator and S is the electronic spin operator. The orbital indices μ, ν run over the p orbitals when atomic site l is occupied by a Se atom, and over the d orbitals when l is occupied by a Nb atom. The SOC intensities at Se and Nb atoms have been adjusted such that the multi-orbital LCAO model with local SOC reproduces as faithfully as possible the energy bands resulting from a fully relativistic DFT calculation. We find that the best fit is given by $\xi_{\text{Nb}} = 79$ meV and $\xi_{\text{Se}} = 211$ meV, in line with those reported in reference 19. Explicit comparison between the LCAO and the DFT bands is given in the supplementary material.

We now apply the RPA method for our multi-orbital tight-binding model. The on-site atomic Coulomb repulsion interaction is given by the Hamiltonian:

$$H = \sum_l U_l \sum_{\mu\nu} \sum_{\sigma\sigma'} a_{l\mu\sigma}^\dagger a_{l\nu\sigma'}^\dagger a_{l\nu\sigma'} a_{l\mu\sigma} \quad (7)$$

where U_l is taken as a free parameter in the calculations, as we have done in the case of the KM Hubbard model. When atomic site l is occupied by a Se atom we take $U_l = 0$. μ, ν are orbital indices running over the d orbitals centered on the Nb sites, and σ_1, σ_2 are spin indices. We find that $U_c = 0.9$ eV marks the critical value of the instability to a ferromagnetic phase.

The $q = 0$ spin susceptibility matrix, calculated within the RPA, using the multi-orbital DFT based TB model are shown in figure 3. We find again a very anisotropic response, with paramagnon enhancement in the \perp channel, much larger than the in-plane spin fluctuations. We also find some quantitative differences. For instance, spin-flip fluctuations are not completely quenched at small energy, in contrast to the KM model. We attribute this difference to the fact that in the multi-orbital DFT based TB model S_z is no longer a conserved quantity and the states away from the K, K' points have a non-negligible mixing of the \uparrow and \downarrow channel. Yet, the main result of this work, the large anisotropy of the spin fluctuations remains.

Some degree of control over the effective Coulomb interaction strength U is available through, for instance, the effective dielectric constant of a conveniently chosen substrate [38, 39]. Its effects can also be controlled indirectly changing the degree of electronic confinement,

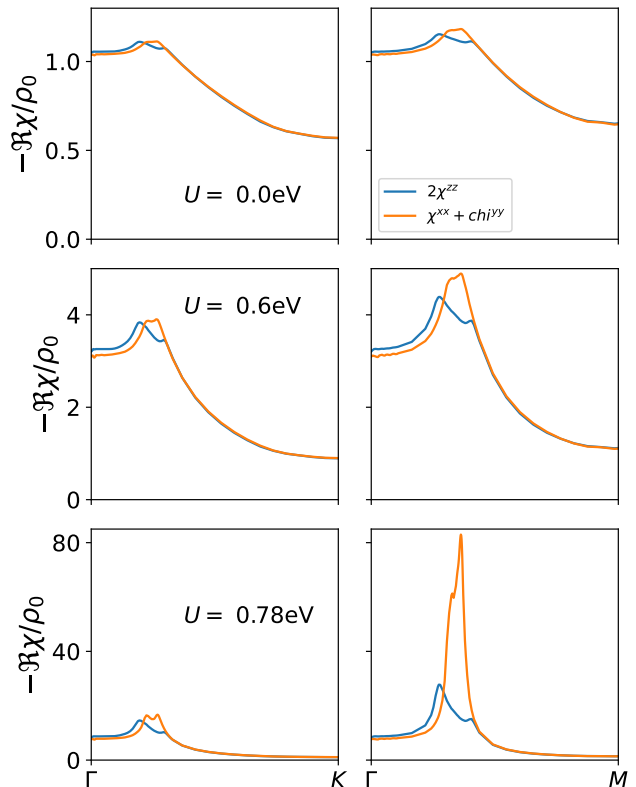


FIG. 4: Transverse ($\chi^{xx} + \chi^{yy}$) and longitudinal (χ^{zz}) spin susceptibilities for 2H-NbSe₂ as functions of wave vector along the $\Gamma - K$ (left panels) and $\Gamma - M$ (right panels) lines, in the static limit ($E = 0$). Top panels are the mean-field results ($U = 0$), the remaining panels show RPA results for different values of the interaction strength U .

either through strain applied to large-area samples [40] or by producing samples of smaller sizes [41].

We now turn to the finite wave vector spin susceptibility in the static limit, directly related to the effective pairing interactions in spin fluctuation mediated superconductivity[42]. In figure 4 we show the real part of the transverse and longitudinal spin susceptibilities at $E = 0$ for 2H-NbSe₂, as a function of wave vector, for different values of U . These results have been obtained using the DFT-derived fermionic hamiltonian for 2H-NbSe₂. Their most prominent feature is the divergency of the *transverse* susceptibility around $q \sim 0.21(2\pi/a_0)$ as U is ramped up, while the longitudinal susceptibility remains finite. Importantly, the divergency here happens for $U \sim 0.8$ eV, which is *significantly smaller* than the corresponding value (~ 0.9 eV) for the uniform ($q = 0$) susceptibility. This indicates that the magnetic instability in 2H-NbSe₂ is actually in-plane, of *spin density wave (SDW) nature*, instead of out-of-plane ferromagnetic. At finite frequencies, we find XY paramagnons: a strong enhancement of the transverse spin fluctuations while longitudinal fluctuations are only modestly enhanced (see

figure 6 on the supplementary material). The strongly anisotropic response and the proximity to a SDW instability may have implications for spin-fluctuation mediated pairing [42]. Qualitatively similar behavior has been analyzed, for instance, in references 43, 44. It is also worth mentioning that the spin fluctuation spectrum of 2H-NbSe₂ depends strongly on the direction of the wave vector, a feature that is relevant to the symmetry of the pairing interactions.

Direct observation of paramagnons, either $q = 0$ Ising paramagnons, or finite q XY paramagnons, with energy and momentum resolution is presently possible only via neutron scattering [45]. However, the applicability of this technique is restricted to bulk samples, due to the very weak neutron-electron interaction (through the dipolar fields produced by their spin magnetic moments). An alternative would be to prepare multilayer samples of NbSe₂ separated by a non-magnetic insulator (such as hexagonal boron nitride, for example). This would preserve the 2D character of the NbSe₂ paramagnons while providing the needed cross-section for neutron scattering.

In conclusion, we have calculated the spin fluctuations of spin-valley coupled systems that describe non-centrosymmetric TMD, such as doped 2H-MoS₂ and 2H-NbSe₂ monolayers. We have used both toy model Hamiltonians, such as the Kane-Mele-Hubbard model, and DFT-based models. We have considered both $q = 0$ and finite q . In all cases we find a very large spin anisotropy of the spin response, driven by the interplay of SOC and lack of inversion symmetry. Remarkably, the magnetic anisotropy of paramagnons is wave-vector dependent, so that we have Ising Paramagnons for $q = 0$ are XY paramagnons for finite q . Our calculations reveal that 2H-NbSe₂ monolayers are closer to SDW instability with in-plane easy axis, rather than a ferromagnetic ($q = 0$) off-plane instability. Our findings can have profound implications for the nature of both the normal state and the superconducting phase of 2H-NbSe₂.

We acknowledge fruitful discussions with Ilya M. Eremin. We acknowledge financial support from the Ministry of Science and Innovation of Spain (grant No. PID2019-109539GB-41), from Generalitat Valenciana (grant No. Prometeo2017/139) and from Fundação Para a Ciência e a Tecnologia, Portugal (grant No. PTDC/FIS-MAC/2045/2021).

* On leave from Departamento de Física Aplicada, Universidad de Alicante, 03690, Sant Vicent del Raspeig, Spain

- [1] T. Moriya, *Spin Fluctuations in Itinerant Electron Magnetism*, Springer Series in Solid-State Sciences, Vol. 56 (Springer, Berlin, Heidelberg, 1985).
- [2] S. Doniach and S. Engelsberg, Phys. Rev. Lett. **17**, 750 (1966).
- [3] P. Lederer and D. L. Mills, Phys. Rev. **165**, 837 (1968).
- [4] N. F. Berk and J. R. Schrieffer, Phys. Rev. Lett. **17**, 433 (1966).
- [5] T. Rice and M. Sigrist, Journal of Physics: Condensed Matter **7**, L643 (1995).
- [6] P. Monthoux, D. Pines, and G. Lonzarich, Nature **450**, 1177 (2007).
- [7] D. Fay and J. Appel, Physical Review B **16**, 2325 (1977).
- [8] C. Pfleiderer, M. Uhlarz, S. Hayden, R. Vollmer, H. v. Löhneysen, N. Bernhoeft, and G. Lonzarich, Nature **412**, 58 (2001).
- [9] Y. Cao, V. Fatemi, S. Fang, K. Watanabe, T. Taniguchi, E. Kaxiras, and P. Jarillo-Herrero, Nature **556**, 43 (2018).
- [10] C. Xu and L. Balents, Phys. Rev. Lett. **121**, 087001 (2018).
- [11] Y.-Z. You and A. Vishwanath, npj Quantum Materials **4**, 16 (2019).
- [12] H. Zhou, T. Xie, T. Taniguchi, K. Watanabe, and A. F. Young, “Superconductivity in rhombohedral trilayer graphene,” (2021), arXiv:2106.07640 [cond-mat].
- [13] Z. Dong and L. Levitov, “Superconductivity in the vicinity of an isospin-polarized state in a cubic dirac band,” (2021), arXiv:2109.01133 [cond-mat].
- [14] S. Ran, C. Eckberg, Q.-P. Ding, Y. Furukawa, T. Metz, S. R. Saha, I.-L. Liu, M. Zic, H. Kim, J. Paglione, *et al.*, Science **365**, 684 (2019).
- [15] D. Wickramaratne, S. Khmelevskiy, D. F. Agterberg, and I. I. Mazin, Physical Review X **10**, 041003 (2020).
- [16] W. Wan, P. Dreher, R. Harsh, F. Guinea, and M. M. Ugeda, arXiv preprint arXiv:2101.04050 (2021).
- [17] A. Hamill, B. Heischmidt, E. Sohn, D. Shaffer, K.-T. Tsai, X. Zhang, X. Xi, A. Suslov, H. Berger, L. Forró, F. J. Burnell, J. Shan, K. F. Mak, R. M. Fernandes, K. Wang, and V. S. Pribiag, Nature Physics **17**, 949 (2021).
- [18] D. Xiao, G.-B. Liu, W. Feng, X. Xu, and W. Yao, Physical Review Letters **108**, 196802 (2012).
- [19] K. Košmider, J. W. González, and J. Fernández-Rossier, Physical Review B: Condensed Matter and Materials Physics **88**, 245436 (2013).
- [20] J. G. Roch, G. Froehlicher, N. Leisgang, P. Makk, K. Watanabe, T. Taniguchi, and R. J. Warburton, Nature nanotechnology **14**, 432 (2019).
- [21] S. Rachel and K. Le Hur, Physical Review B **82**, 075106 (2010).
- [22] D. Soriano and J. Fernández-Rossier, Physical Review B **82**, 161302(R) (2010).
- [23] Y. Fukaya, K. Yada, A. Hattori, and Y. Tanaka, Journal of the Physical Society of Japan **85**, 104704 (2016).
- [24] X. Wu, M. Fink, W. Hanke, R. Thomale, and D. Di Sante, Physical Review B **100**, 041117(R) (2019).
- [25] A. T. Costa, R. B. Muniz, S. Lounis, A. B. Klautau, and D. L. Mills, Phys. Rev. B **82**, 014428 (2010).
- [26] A. T. Costa, D. L. R. Santos, N. M. R. Peres, and J. Fernández-Rossier, 2D Mater. **7**, 045031 (2020).
- [27] C. L. Kane and E. J. Mele, Physical Review Letters **95**, 226801 (2005).
- [28] P. Hohenberg and W. Kohn, Phys. Rev. **136**, B864 (1964).
- [29] W. Kohn and L. J. Sham, Phys. Rev. **140**, A1133 (1965).
- [30] P. Giannozzi, O. Andreussi, T. Brumme, O. Bunau, M. B. Nardelli, M. Calandra, R. Car, C. Cavazzoni, D. Ceresoli, M. Cococcioni, N. Colonna, I. Carnimeo, A. D. Corso, S. de Gironcoli, P. Delugas, R. A. D. Jr,

- A. Ferretti, A. Floris, G. Fratesi, G. Fugallo, R. Gebauer, U. Gerstmann, F. Giustino, T. Gorni, J. Jia, M. Kawamura, H.-Y. Ko, A. Kokalj, E. Küçükbenli, M. Lazzeri, M. Marsili, N. Marzari, F. Mauri, N. L. Nguyen, H.-V. Nguyen, A. O. de-la Roza, L. Paulatto, S. Poncé, D. Rocca, R. Sabatini, B. Santra, M. Schlipf, A. P. Seitsonen, A. Smogunov, I. Timrov, T. Thonhauser, P. Umari, N. Vast, X. Wu, and S. Baroni, *Journal of Physics: Condensed Matter* **29**, 465901 (2017).
- [31] J. P. Perdew, K. Burke, and M. Ernzerhof, *Phys. Rev. Lett.* **77**, 3865 (1996).
- [32] G. Kresse and D. Joubert, *Phys. Rev. B* **59**, 1758 (1999).
- [33] A. D. Corso, *Computational Materials Science* **95**, 337 (2014).
- [34] Y. Zhou, Z. Wang, P. Yang, X. Zu, L. Yang, X. Sun, and F. Gao, *ACS Nano* **6**, 9727 (2012).
- [35] L. A. Agapito, A. Ferretti, A. Calzolari, S. Curtarolo, and M. Buongiorno Nardelli, *Phys. Rev. B* **88**, 165127 (2013).
- [36] L. A. Agapito, S. Curtarolo, and M. Buongiorno Nardelli, *Phys. Rev. X* **5**, 011006 (2015).
- [37] M. B. Nardelli, F. T. Cerasoli, M. Costa, S. Curtarolo, R. D. Gennaro, M. Fornari, L. Liyanage, A. R. Supka, and H. Wang, *Computational Materials Science* **143**, 462 (2018).
- [38] A. Raja, A. Chaves, J. Yu, G. Arefe, H. M. Hill, A. F. Rigosi, T. C. Berkelbach, P. Nagler, C. Schüller, T. Korn, C. Nuckolls, J. Hone, L. E. Brus, T. F. Heinz, D. R. Reichman, and A. Chernikov, *Nature Communications* **8**, 15251 (2017).
- [39] E. G. C. P. van Loon, M. Schüler, D. Springer, G. Sangiovanni, J. M. Tomczak, and T. O. Wehling, “Coulomb engineering of two-dimensional mott materials,” (2020), arXiv:2001.01735 [cond-mat.str-el] .
- [40] Y. Yan, S. Ding, X. Wu, J. Zhu, D. Feng, X. Yang, and F. Li, *RSC Adv.* **10**, 39455 (2020).
- [41] S. C. Ganguli, V. Vaño, S. Kezilebieke, J. L. Lado, and P. Liljeroth, *Nano Letters* **0**, null (0), pMID: 35167310, <https://doi.org/10.1021/acs.nanolett.1c03491> .
- [42] M. Sigrist, *AIP Conference Proceedings* **789**, 165 (2005), <https://aip.scitation.org/doi/pdf/10.1063/1.2080350> .
- [43] A. T. Rømer, I. Eremin, P. J. Hirschfeld, and B. M. Andersen, *Phys. Rev. B* **93**, 174519 (2016).
- [44] A. T. Rømer, D. D. Scherer, I. M. Eremin, P. J. Hirschfeld, and B. M. Andersen, *Phys. Rev. Lett.* **123**, 247001 (2019).
- [45] R. Double, S. M. Hayden, P. Dai, H. A. Mook, J. R. Thompson, and C. D. Frost, *Phys. Rev. Lett.* **105**, 027207 (2010).

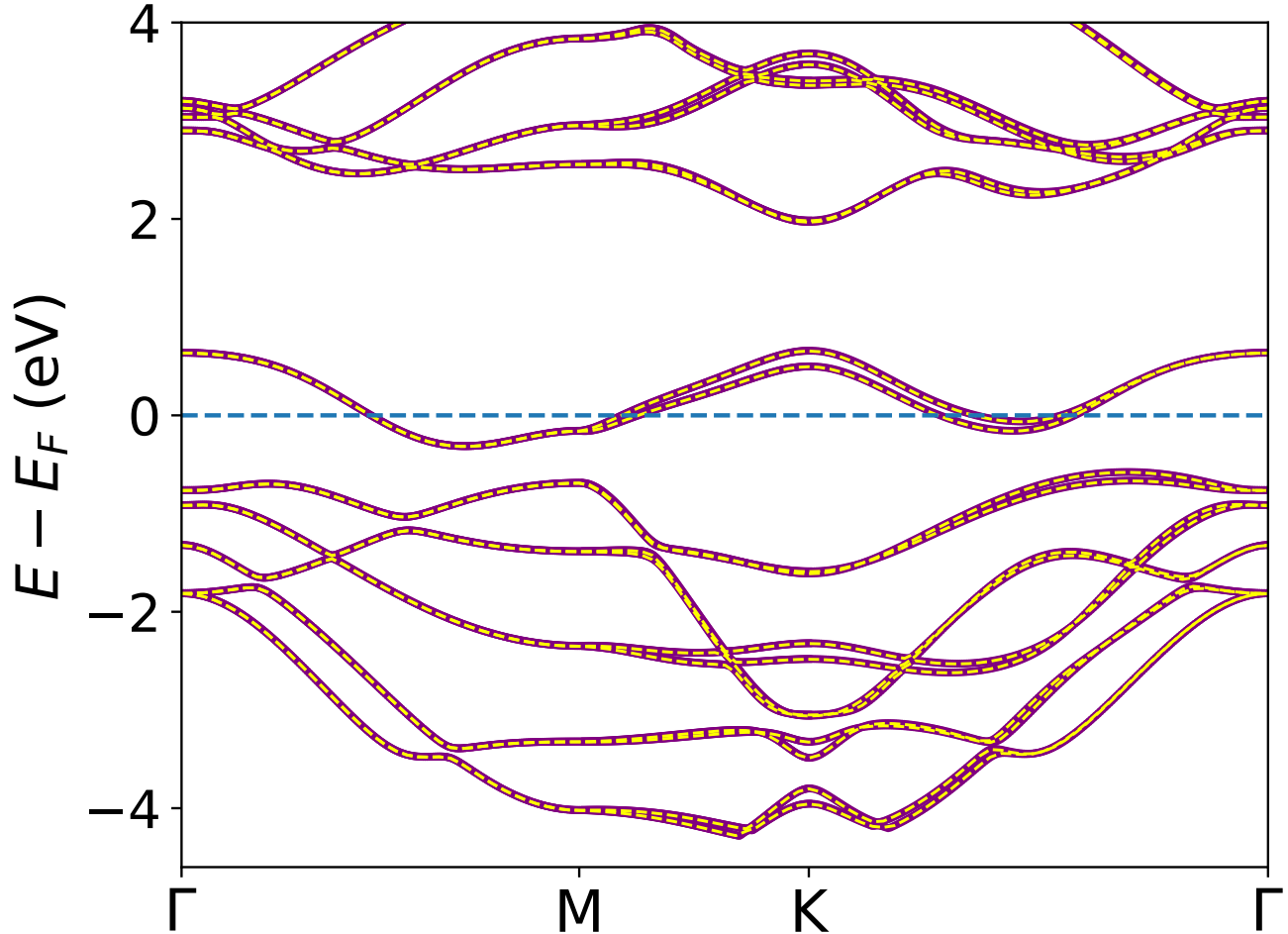


FIG. 5: Comparison between the band structure provided by the fully relativistic DFT calculation described in the main text (dashed yellow lines) and the energy bands generated by the a tight-binding-like hamiltonian, including local spin-orbit coupling (purple symbols).

Further details regarding the electronic structure of monolayer 2H-NbSe₂

Here we provide additional plots showing results for the DFT calculation and the associated multiorbital tight-binding model. We show in figure 5 that the multiorbital model derived from the DFT calculation, supplemented by a local spin-orbit coupling term, fits exceedingly well the DFT bands.

In figure 6 we show the local density of states around the Fermi level, projected on the Nb site. We also show how the energy eigenstates around the Fermi level have predominantly *d* character. From the *d*-projected LDOS it can also be inferred that the critical U for which the spin-unpolarized ground state becomes unstable (to a spatially uniform perturbation) is $U_c \approx 0.93$ eV. Notice, however, that the non-uniform transverse susceptibility diverges at a finite wave vector for values of U that are considerably smaller than that.

Paramagnon spectra at finite wave vectors

In figure 7 we show the longitudinal spin spectral density as a function of wave vector and energy. These results have been obtained with the multi-orbital model extracted from the DFT calculation. As wave vector increases, the energy at which the spectral density peaks also increases; by following this peak we extract a “paramagnon dispersion relation,” which can serve as a guide for the observation of the Ising paramagnons of NbSe₂ in experiments.

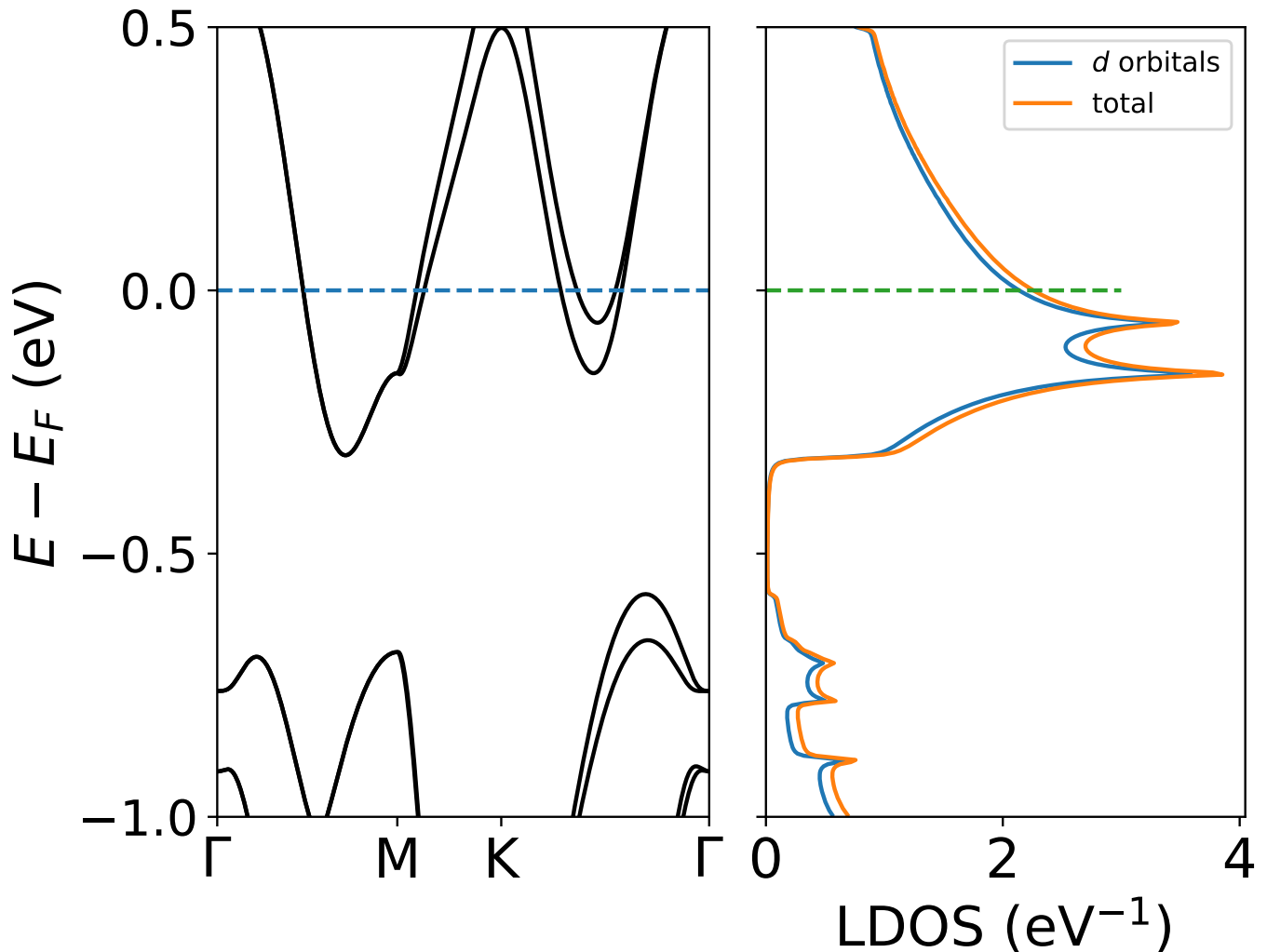


FIG. 6: Detail of the band structure (left) and local density of states at Nb sites (right) around the Fermi level E_F for a NbSe₂ monolayer. We also show the LDOS projected on the d orbitals (right panel, blue curve). These results were obtained using the PAO hamiltonian, and include SOC.

In figure 8 we show the transverse and longitudinal components of the spin susceptibility for the toy model, at zero excitation energy, as a function of wave vector. The spin-valley locking leads to large differences between the two responses. The features of these response functions can be associated to nesting vectors connecting different portions of the Fermi surface (FS), as shown in figure 9. The vector connecting parallel portions of the FS with the same spin polarization, δk_{\parallel} , is associated with the region over which the longitudinal mean-field ($U = 0$) susceptibility χ^{zz} is flat. The kink seen in the transverse component ($\chi^{xx} + \chi^{yy}$) at a finite wave vector along $\Gamma - K$ is associated with the wave vector connecting portions of the FS with opposite spins, δk_{\perp} .

In figure 10 we show the transverse and longitudinal spin fluctuation spectra at three different wave vectors along the $\Gamma - M$ line, for $U = 0.79$ eV. Besides being strongly enhanced, transverse fluctuations clearly dominate the spectrum in this region of the Brillouin zone, prompting us to identify the existence of XY paramagnons.

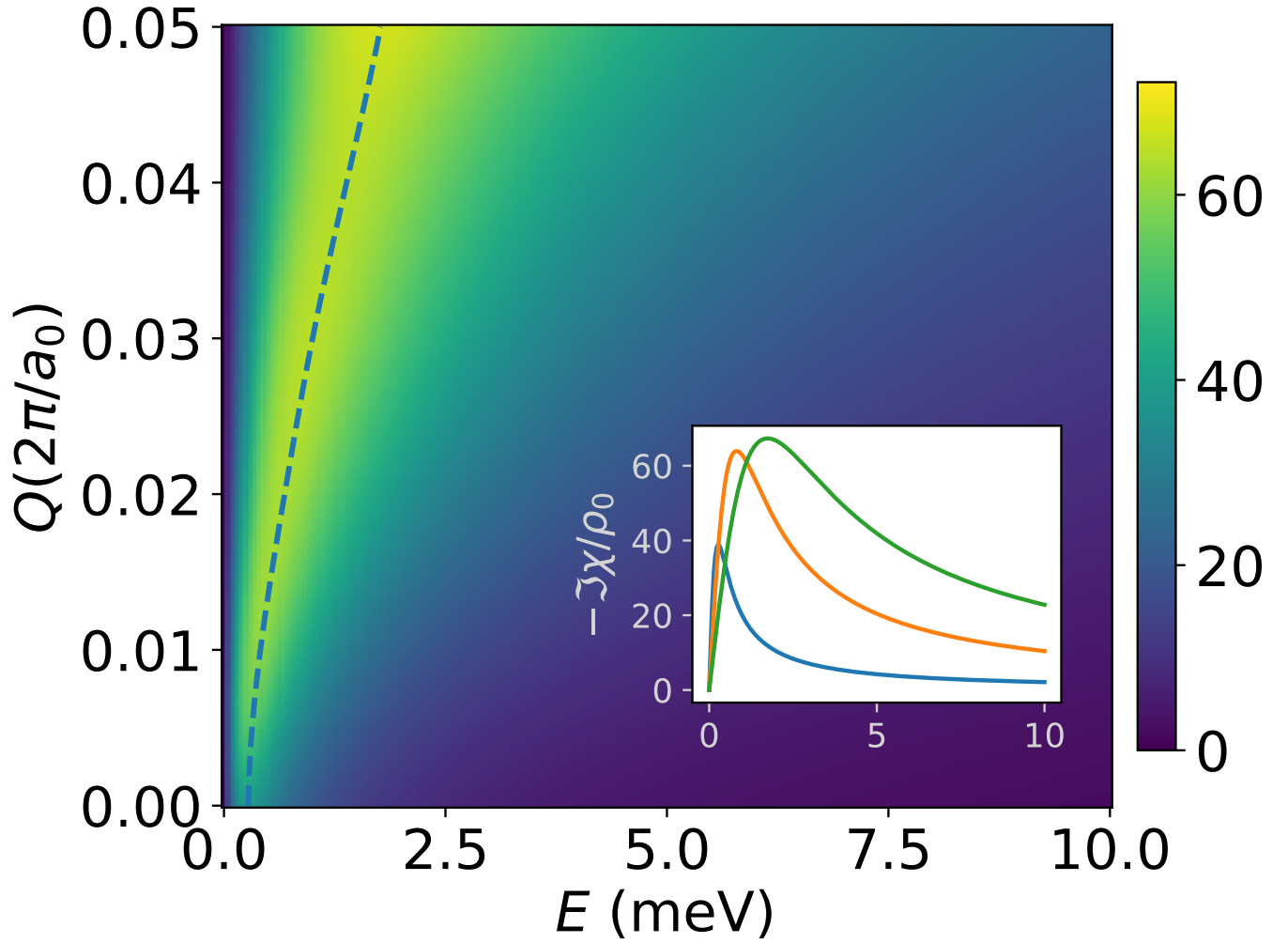


FIG. 7: Density plot of the spectral density of longitudinal spin fluctuations in monolayer NbSe₂ as a function of energy and wave vector for $U = 0.88$ eV. The dashed line marks the positions of the maxima of the spectral density. The inset shows the same spectral density as a function of energy for three values of the wave vector (along $\Gamma - K$): 0 (blue curve), $0.01(2\pi/a_0)$ (orange curve) and $0.05(2\pi/a_0)$ (green curve).

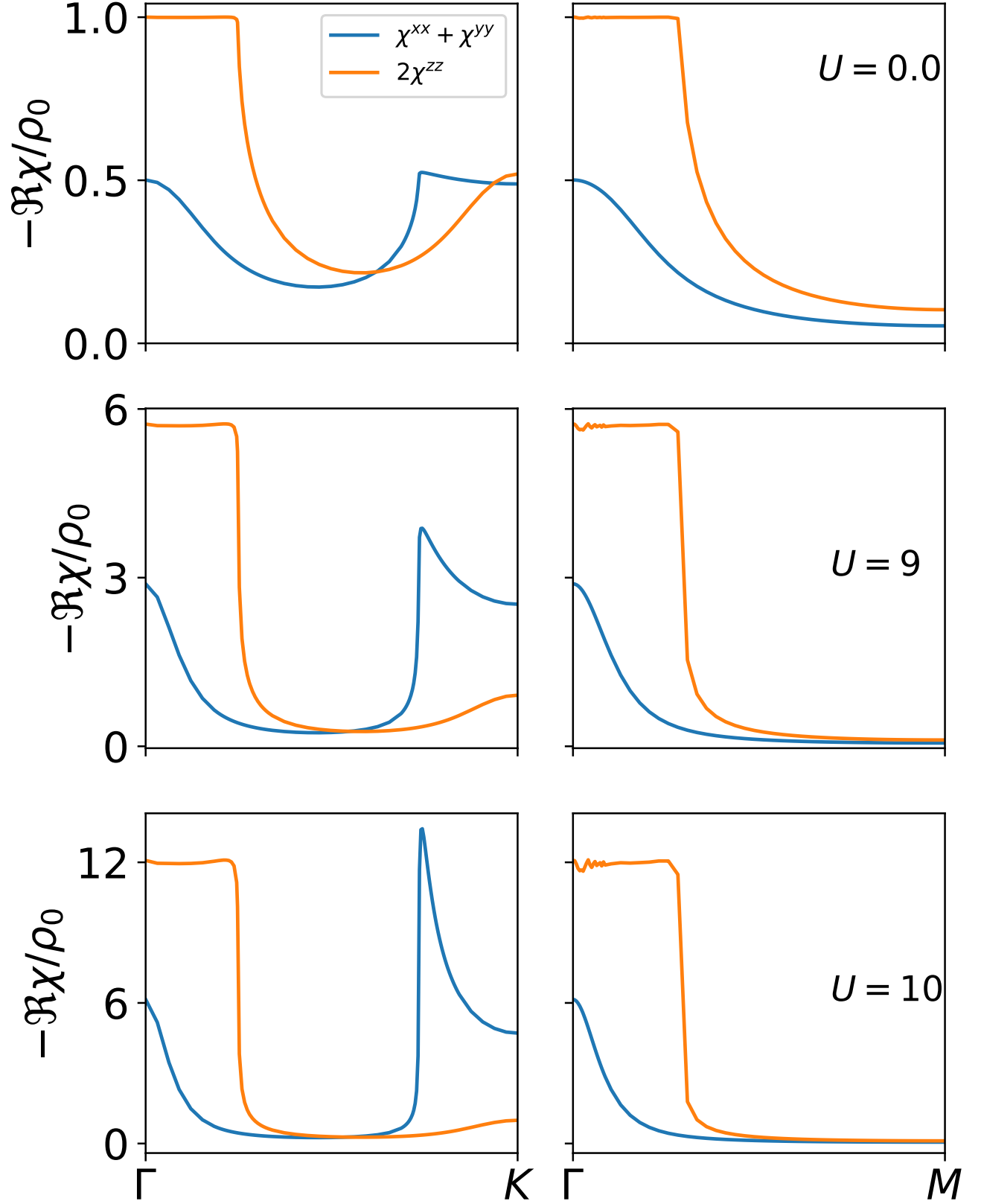


FIG. 8: Transverse ($\chi^{xx} + \chi^{yy}$) and longitudinal (χ^{zz}) spin susceptibilities for the Kane-Mele-Hubbard model as functions of wave vector along the $\Gamma - K$ (left panels) and $\Gamma - M$ (right panels) lines, in the static limit ($E = 0$). Top panels are the mean-field results ($U = 0$), the remaining panels show RPA results for different values of the interaction strength U .

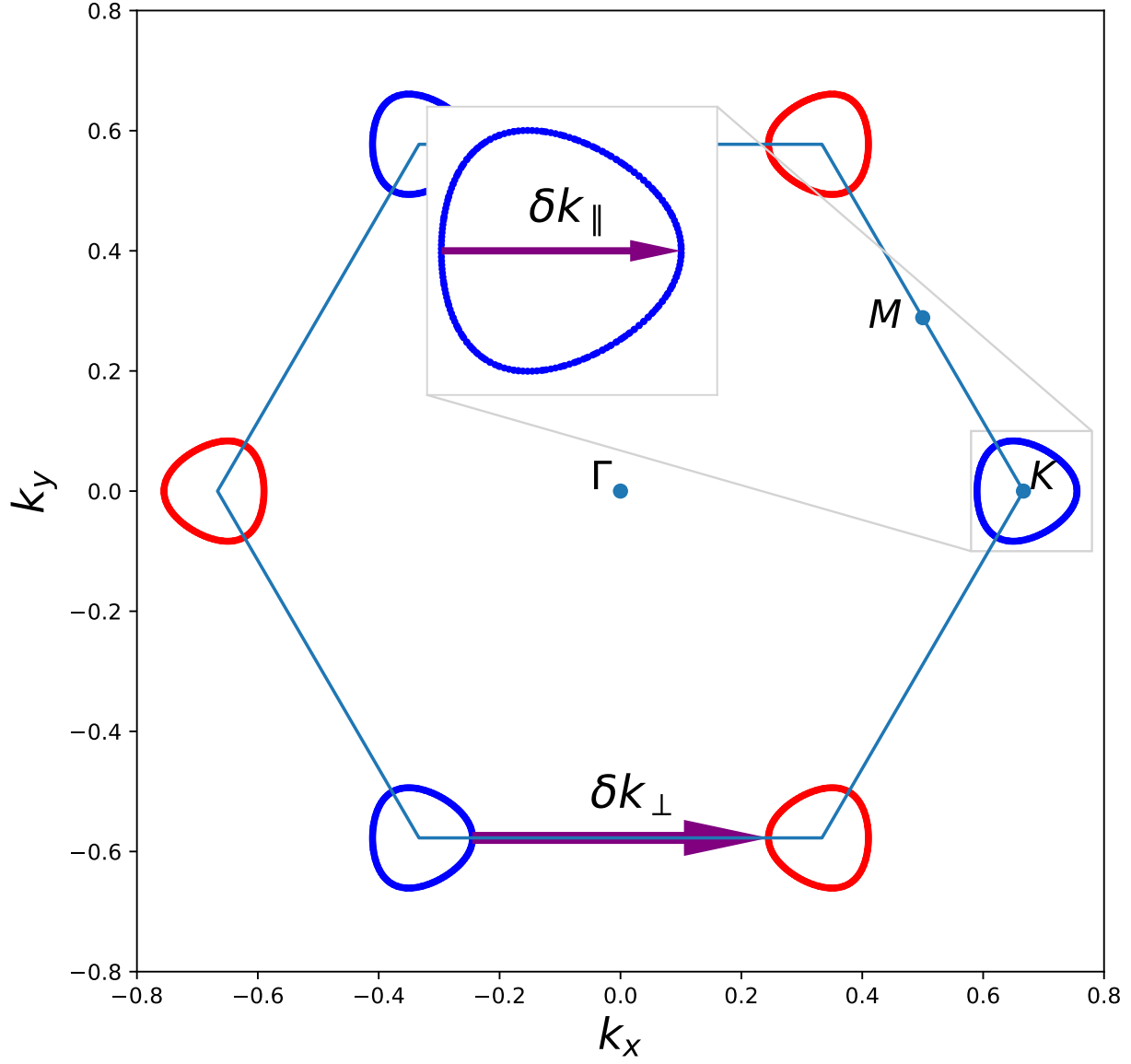


FIG. 9: Fermi surface for the Kane-Mele-Hubbard model for $E_F = 3t$. The width of the pockets around the K points (δk_{\parallel}) correspond to the region in which $\Re\chi^{zz}(Q, 0)$ is almost flat (see figure 4). The length of the nesting vector connecting opposite-spin pockets around K and K' (δk_{\perp}) corresponds to the position of the peak in $\chi^{xx} + \chi^{yy}$ along $\Gamma - K$.

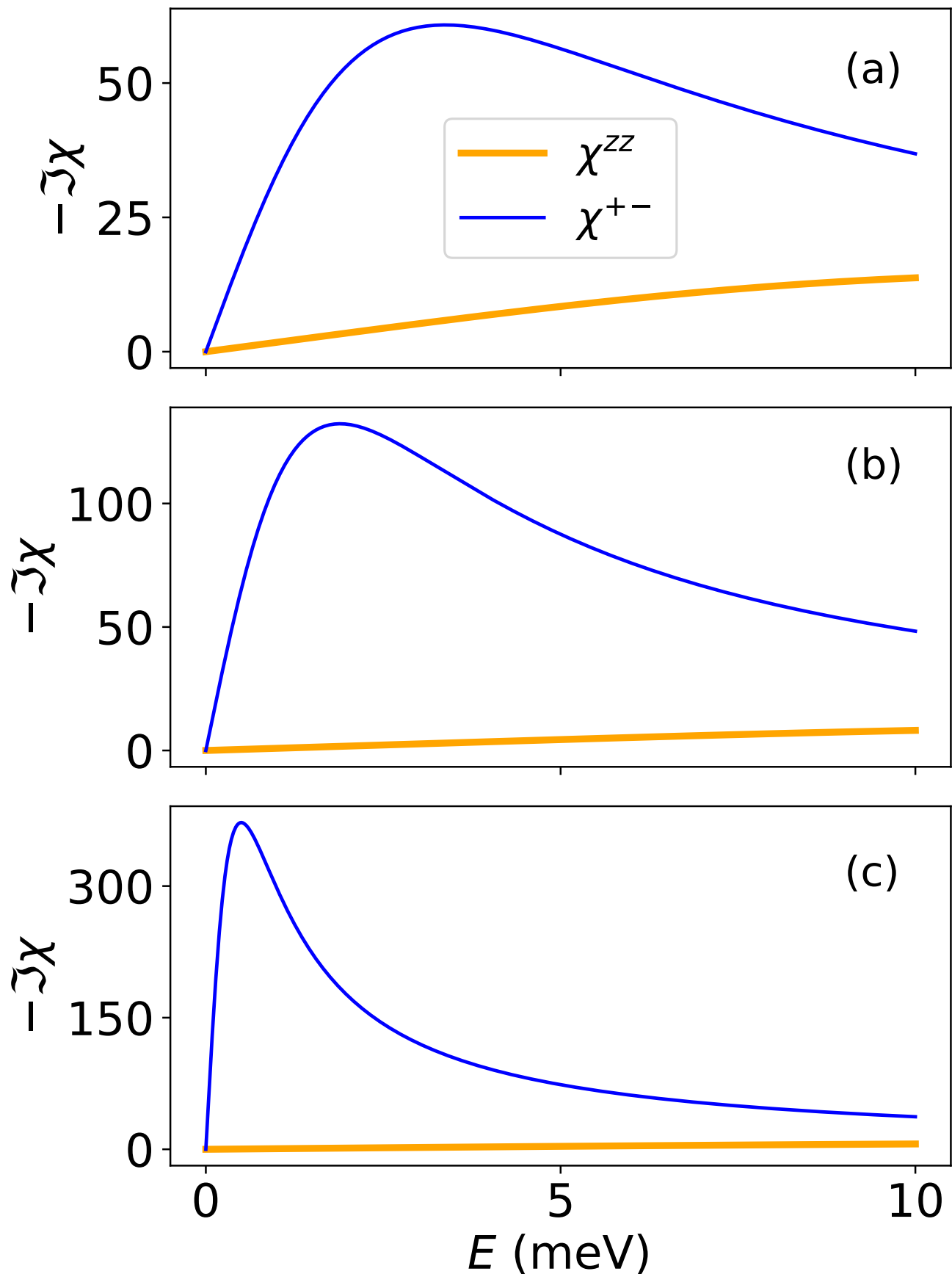


FIG. 10: Transverse (χ^{+-} , blue curve) and longitudinal (χ^{zz} , orange) spin fluctuation spectral densities at $q = 0.18(2\pi/a_0)$ (a), $q = 0.20(2\pi/a_0)$ (b) and $q = 0.21(2\pi/a_0)$ (c), along the $\Gamma - M$ line, for $U = 0.79$ eV.